THE JOURNAL OF PHYSICAL CHEMISTRY LETTERS
A JOURNAL OF THE AMERICAN CHEMICAL SOCIETY

pubs.acs.org/JPCL

Letter

Vanishing Confinement Regime in Terahertz HgTe Nanocrystals Studied under Extreme Conditions of Temperature and Pressure

Stefano Pierini, Francesco Capitani, Michael Scimeca, Sergei Kozlov, Debora Pierucci, Rodolphe Alchaar, Claire Abadie, Adrien Khalili, Mariarosa Cavallo, Tung Huu Dang, Huichen Zhang, Erwan Bossavit, Charlie Gréboval, José Avila, Benoit Baptiste, Stefan Klotz, Ayaskanta Sahu, Cheryl Feuillet-Palma, Xiang Zhen Xu, Abdelkarim Ouerghi, Sandrine Ithurria, James K. Utterback, Sebastien Sauvage, and Emmanuel Lhuillier*

Cite This: *J. Phys. Chem. Lett.* 2022, 13, 6919−6926

Read Online

ACCESS | Metrics & More | Article Recommendations | Supporting Information

ABSTRACT: While HgTe nanocrystals (NCs) in the mid-infrared region have reached a high level of maturity, their far-infrared counterparts remain far less studied, raising the need for an in-depth investigation of the material before efficient device integration can be considered. Here, we explore the effect of temperature and pressure on the structural, spectroscopic, and transport properties of HgTe NCs displaying an intraband absorption at 10 THz. The temperature leads to a very weak modulation of the spectrum as opposed to what was observed for strongly confined HgTe NCs. HgTe NC films present ambipolar conduction with a clear prevalence of electron conduction as confirmed by transistor and thermoelectric measurements. Under the application of pressure, the material undergoes phase transitions from the zinc blende to cinnabar phase and later to the rock salt phase which we reveal using joint X-ray diffraction and infrared spectroscopy measurements. We discuss how the pressure existence domain of each phase is affected by the particle size.

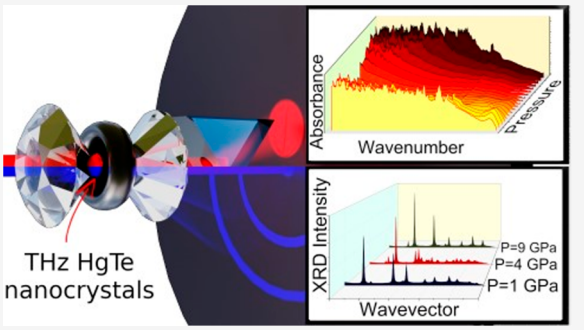

HgTe nanocrystals[1,2] (NCs) have reached a high level of maturity that enables their use in complex devices such as lasers,[3] light-emitting diodes (LEDs),[4−6] infrared (IR) sensors with carrier density[7−10] light−matter control,[11−14] and cameras.[15−17] All of these results have been obtained with NCs absorbing in the near- and mid-wave infrared range. Because of the semimetal nature of HgTe, the absorption spectrum of NCs can be tuned up to the terahertz (THz) frequency range, which corresponds to the spectral range in which the NC properties remain underexplored.[18] Goubet et al. reported a strategy for growing large HgTe NCs[19] that are larger than the Bohr radius[20] (40 nm), which is large compared to other II−VI semiconductors due to the high dielectric constant and low effective electron mass of HgTe. They demonstrated that, in the THz range, absorption occurs through an intraband transition[15,21−25] whose maximum can be increased to 60 μm (20 meV, 166 cm^{-1}, or 5 THz). Later, Apretna et al. investigated the carrier dynamics in such THz-absorbing HgTe NCs.[26] They found that intraband relaxation occurs within a few picoseconds and with a decay rate of 0.5 eV ps^{-1}, which is close to the values observed in more strongly confined HgTe NCs with sparser densities of states.[4,27]

The THz HgTe NCs offer an interesting playground for probing an electronic state between the bulk and the strongly confined regimes.[28] Here, we explore how temperature and pressure affect the structural and electronic properties of an HgTe NC assembly in this intermediate regime where confinement is almost nonexistent.

The phase diagram of HgTe as a function of pressure and temperature has been extensively investigated in the bulk[29−31] and thin film[32] forms. The material is known to experience a series of structural phase changes as pressure is applied. The zinc blende phase, stable at room pressure, is a semimetal phase, which transforms into a semiconductor when confinement is introduced. Under higher pressure, the material turns[29−31] to the cinnabar phase and then to the rock salt phase, which are a semiconductor and a metallic phase, respectively. Here, we show that the intraband feature in the THz range appears to be quite stable over the explored temperature range and discuss how the structural phases of HgTe have their domain of existence affected by the finite particle size.

Received: May 30, 2022
Accepted: July 18, 2022
Published: July 22, 2022

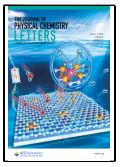

https://doi.org/10.1021/acs.jpclett.2c01636
J. Phys. Chem. Lett. 2022, 13, 6919−6926

We start by growing large HgTe NCs presenting intraband absorption at ≈300 cm^{-1} or 10 THz (see Figure 1b). Above

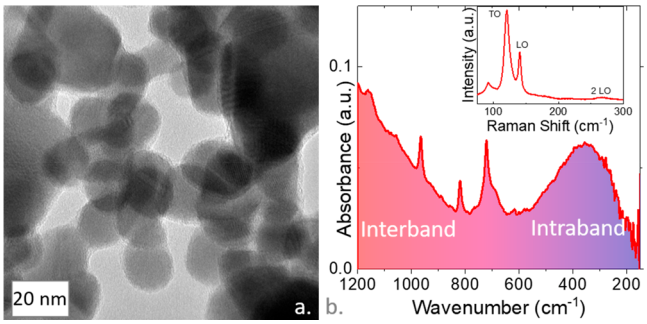

Figure 1. Structural and spectroscopic properties of THz HgTe NCs. (a) TEM image of THz HgTe NCs. (b) Infrared spectrum of THz HgTe NCs. The inset shows the Raman spectrum of THz HgTe NCs.

800 cm^{-1}, we observe an increase in the absorption that can be attributed to interband absorption. The Raman spectrum (see the inset of Figure 1b) displays two main features associated with optical phonons that are the TO phonon at 120 cm^{-1} and the LO phonon at 141 cm^{-1}. Thus, we can confidently attribute the remaining narrow peaks [from 700 to 1000 cm^{-1} (see Figures S2 and S3)] observed in the infrared spectrum to organic bonds coming from ligands. Electron microscopy (Figure 1a and Figure S1) shows particles ∼15 nm in size, which is also confirmed by the Scherrer length obtained by fitting the line width of the X-ray diffraction pattern (see Figure S5).

We then explore the effect of temperature on the spectral and transport properties of these HgTe NCs (see Figure 2). In

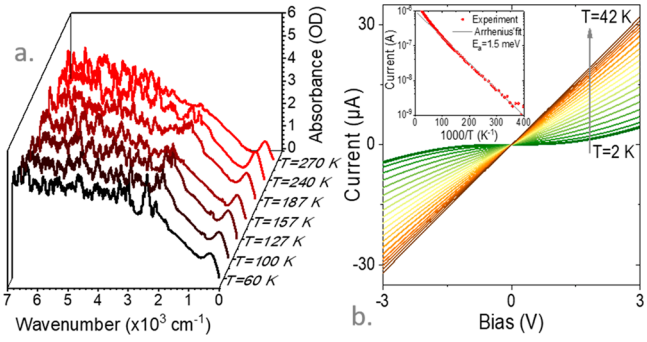

Figure 2. Impact of temperature. (a) Infrared spectra of THz HgTe NCs obtained at various temperatures. (b) $I-V$ curves from a thin film of THz HgTe NCs at various temperatures from 2 to 42 K in steps of 2 K. Curves at higher temperatures are given in Figure S1. The inset shows the current as a function of temperature under a constant drain source bias (V = 100 mV). A fit of the curve to the Arrhenius equation leading to a 1.5 meV activation energy is also provided.

the range from 300 to 60 K, the infrared absorption spectrum displays very limited changes with neither a shift nor a broadening of the intraband signal (see Figure 2a). It has been previously reported in HgSe NCs, also displaying intraband absorption,[33] that such a transition indeed presents a weak temperature dependence. The temperature-induced shift was also observed to be weaker for less confined particles.[33] In this temperature range, where thermal energy k_BT is in the range of 5−25 meV, the thermal activation of carriers remains high, and no narrowing of the optical feature is observed.

Once the NCs were capped with short ligands, here a mixture of mercaptoethanol and $HgCl_2$ ions,[34,35] the $I-V$ curves were measured over the range of 2−300 K (see Figure 2b and Figure S4). Above 20 K, $I-V$ curves present ohmic character. Below this value, the curves acquire a superlinear behavior, characteristic of transport in semiconductors at low temperatures. The current as a function of temperature (inset of Figure 2b) follows an Arrhenius behavior over the whole temperature range. The associated activation energy is determined to be 1.5 meV. This value is consistent with the particle charging energy[36] (E_C) for these particles, which is given by the expression $E_C = \frac{e^2}{4\pi\varepsilon_0\varepsilon_r}\frac{s}{(R+s)R}$ = 1.1 meV, where ε_0 is the vacuum permittivity, ε_r is the dielectric constant[37] of HgTe (15.2), R is the particle radius (7 nm), s is the particle spacing (1.5 nm) and e the electron charge.

We then add a gate to the system to control the carrier density and determine the nature of the majority carriers. At room temperature, we use electrolyte gating that enables low driving biases thanks to its large capacitance. In this case, the transfer curve appears to be ambipolar with conduction under both negative (i.e., hole injection) and positive (i.e., electron injection) gate biases (see Figure 3a). There is nevertheless a

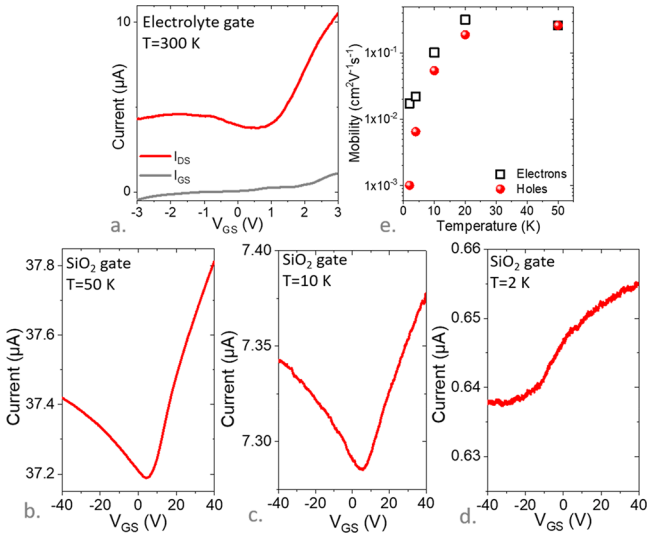

Figure 3. Transistor measurements. (a) Transfer curve (i.e., drain and gate current as a function of the applied gate bias under a constant drain source bias V_{DS} of 0.05 V) for THz HgTe NCs gated with an electrolyte at room temperature. Transfer curves (i.e., drain and gate current as a function of the applied gate bias under a constant drain source bias V_{DS} of 1 V) for THz HgTe NCs with a back silica substrate (t_{SiO_2} = 300 nm) at (b) 50 K, (c) 10 K, and (d) 2 K. (e) Electron and hole mobilities as a function of temperature.

clear prevalence for electron conduction. This is consistent with a degenerated electron doping through the observation of intraband absorption. Furthermore, we have performed thermoelectric measurements to determine the sign and magnitude of the Seebeck coefficient, which we found to be −83 ± 3 $\mu V\ K^{-1}$. This negative Seebeck coefficient further confirms the n-type nature of the material.[35] Second, for interband MWIR-absorbing HgTe samples, we also observe a negative Seebeck coefficient (typically approximately −301 ± 9

https://doi.org/10.1021/acs.jpclett.2c01636
J. Phys. Chem. Lett. 2022, 13, 6919−6926

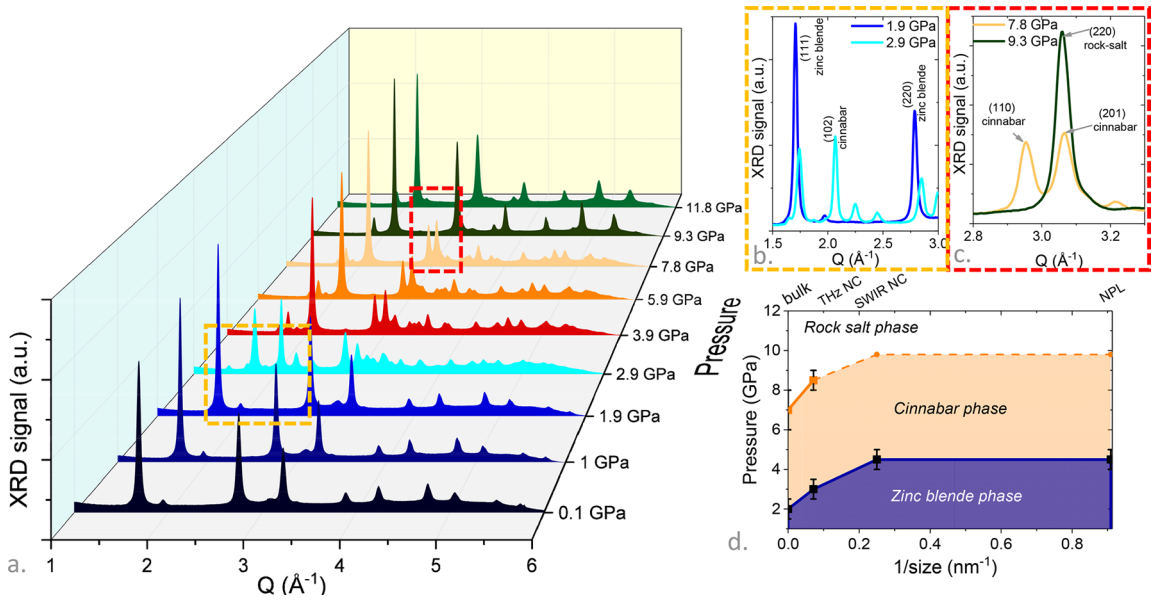

Figure 4. Structural phase changes in THz HgTe NCs probed by diffraction. (a) X-ray diffraction (XRD) pattern for THz HgTe NCs at room temperature and under various pressures. (b) Close-up of the XRD pattern for two pressures around the transition from the zinc blende to cinnabar phase. (c) Close-up of the XRD pattern for two pressures around the transition from the cinnabar to rock salt phase. (d) Threshold pressures for the zinc blende to cinnabar and cinnabar to rock salt phase transitions for various sizes of HgTe. The solid line shows the experimental data. The dashed line is extrapolated to match the dependence of the zinc blende to cinnabar phase transition. Values for the bulk were taken from ref 38. Data for short-wave infrared HgTe NCs were taken from ref 45. Data for HgTe nanoplatelets (NPLs) were taken from ref 28.

μV K^{-1}), proving that electron transport dominates conduction. However, a lower absolute value of the Seebeck coefficient for the THz-absorbing dots confirms that these are degenerately doped and demonstrates intraband absorption, thus validating the optical measurements.

At low temperatures, we switch to a more conventional dielectric gating based on SiO_2, because ion freezing occurring in electrolyte induces a loss of the gate effect. Down to 10 K, the transport preserves its ambipolar character (see Figure 3b,c), though the current modulation becomes weak. At very low temperatures, below 4 K, we observe that the transfer curve displays electron conduction only. This may result from a shift in the Fermi level deeper in the conduction band, but a freezing of the holes due to their large mass cannot be excluded.

Mobility values were extracted using the expression $\mu = \frac{L}{WC_{\Sigma}V_{ds}}\frac{\partial I_{ds}}{\partial V_{gs}}$, where L is the distance between the electrodes, W their length, and C_{Σ} the capacitance. The mobilities, as shown in Figure 3e, appear to be thermally activated. At 40 K, electron and hole mobilities reach 0.3 cm^2 V^{-1} s^{-1} and decrease to 10^{-3} cm^2 V^{-1} s^{-1} at 2 K.

We then explored the impact of pressure and conducted a joint structural and spectroscopic investigation. HgTe under pressure is known to experience a series of structural phase transitions:[29−31] zinc blende to cinnabar (threshold pressure[31,38] $P_{ZB\rightarrow cinn}$ of 1.5−2.5 GPa) and then to rock salt above a $P_{cinn\rightarrow RS}$ of 6−8 GPa. These transitions occur at a fairly low pressure compared to what is observed in CdSe[39−42] (the transition from wurtzite to rock salt occurs in the range of 3.6−5 GPa) or PbS[43,44] NCs (no transition below 8 GPa). Such low pressure-induced phase changes might be critical regarding a core−shell structure growth since structure because the lattice mismatch between the core and the shell could generate a strain-inducing undesired phase change.

A series of X-ray diffraction patterns were acquired for pressures ranging from 0 to 12 GPa at room temperature (see Figure 4a and Figure S6) to monitor the structural phase change. The transition to the cinnabar phase is observed at ∼2.9 GPa, as shown in detail in Figure 4b. The amplitudes of the peaks associated with the (111) and (200) planes (q = 1.5−3 Å^{-1}) of the zinc blende phase drastically decrease as the pressure is increased, and the (102) peak of the cinnabar phase appears. There is clearly a range of pressures where both phases are present. The transition toward the rock salt is better illustrated in Figure 4c, where the peaks related to the (110) and (201) planes of the cinnabar are transformed into a single peak attributed to the (220) plane of the rock salt phase.

As may have been anticipated,[39−42] the threshold pressures are intermediate between the values observed for the bulk[38] and those observed for strongly confined forms of HgTe NCs.[28,45] In Figure 4d, we present a phase diagram that shows how the finite size affects the stability range of each phase as a function of the particle size. In the case of CdSe, the pressure shift observed for smaller sizes has been attributed to additional surface energy as the particle size decreases.[39−42]

As a result of the structural phase change, electronic phase changes have been observed[46] and predicted[31] in the bulk but remain unexplored in the case of NCs. The zinc blende phase of HgTe is a semimetal (i.e., a gapless semiconductor) in bulk form, while the cinnabar and rock salt phases are a semiconductor and a metal, respectively. We thus acquire a series of infrared spectra in the range of 0−10 GPa, which corresponds to the range of existence of the three phases. To better observe the appearance and disappearance of a band gap, we use a broadband setup (7000−200 cm^{-1}) for which a schematic is proposed in Figure S7.

The zinc blende absorption spectrum (Figures 1b and 5a) presents the intraband feature around 300 cm^{-1} and a long intense tail relative to the interband transitions in the mid-

https://doi.org/10.1021/acs.jpclett.2c01636
J. Phys. Chem. Lett. 2022, 13, 6919−6926

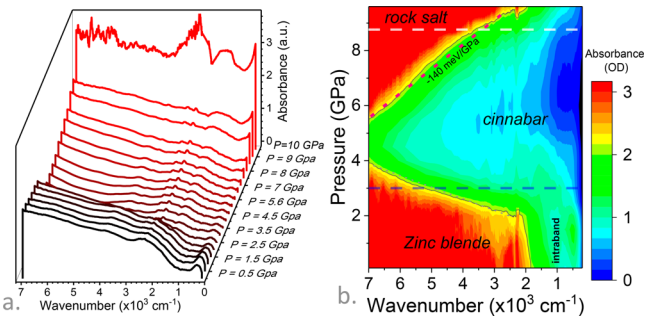

Figure 5. Electronic phase change in THz HgTe NCs probed by infrared spectroscopy under pressure. (a) Infrared spectra for THz HgTe NCs under various pressures, made at room temperature. Data obtained at 60 K are given in Figure S9. (b) Infrared absorbance as a function of wavenumber and pressure for measurements conducted at 60 K. The thick dashed lines correspond to threshold pressure for structural phase changes. The pink dotted lined shows the dependence of the band gap in the zinc blende and cinnabar phases.

infrared range. In the zinc blende phase, the pressure dependence of the interband absorption observed in Figure 5 is qualitatively consistent with our previous modeling of HgTe nanocrystals and nanoplatelets under pressure using a multiband k.p formalism.[28] Quantitatively, as shown in Figure S10, we observe a blue shift of roughly 30 meV GPa^{-1} of the interband absorption with pressure. Using the 14-band k.p modeling of ref 28, fitted to small HgTe nanocrystals and nanoplatelets, we predict a shift of 32 meV GPa^{-1} at 60 K for the large nanocrystals. Considering the difficulty of precisely pinpointing the interband absorption, the predicted energy shifts with pressure are in reasonable agreement with the spectroscopy, consolidating the set of pressure parameters that we use in the modeling.[28]

Above 2.5 GPa, the overall absorption signal collapses (see Figure 5a), which results from the opening of a band gap in the bulk cinnabar phase.[31] Within this phase, we observe a clear red shift of the band gap with pressure (i.e., a band gap closing) (also see Figure 5b). We found $\frac{dE_{cinn}}{dP} = -139$ meV GPa^{-1}, close to the value determined from transport measurements on the bulk[46] (−159 meV GPa^{-1}). This behavior is drastically different from the pressure dependence of the interband feature in the zinc blende phase for which an opening of the band gap was observed.[45] However, the latter effect was the result of the pressure on the quantum confinement through a modification of the effective mass of the electrons. Further exploration of this phase, in particular at an even lower temperature, will be of utmost interest because the latter has been observed to be superconductive around 6 K.[47]

In the rock salt phase, the sample becomes strongly absorbent and the spectrum becomes almost saturated over the whole spectral range. We attribute this behavior to the transition toward the metallic phase.

To conclude, we have explored the effect of temperature and pressure on the structural, spectroscopic, and transport properties of 10 THz absorbing HgTe NCs. In the zinc blende phase, the particles display both interband and intraband absorption, which is consistent with the degenerate n-type nature also observed from transistor and thermoelectric measurements. The narrow band gap nature of the material enables both electron and hole conduction from room temperature down to 10K, and in this range, the absorption spectrum is barely affected by the temperature (i.e., neither a narrowing nor a shift of the intraband feature). Only at very low temperatures (≤4 K) we do observe a change in behavior with the loss of hole conduction. Pressure impacts the structure and spectral properties in a far more dramatic way. As seen for the bulk, HgTe NCs experience a series of phase changes from the zinc blende/semimetallic phase to the cinnabar/semiconductive phase and finally to the rock salt/metallic phase. The domain of existence of the different phases appears to be shifted toward higher pressures with respect to the bulk, and we provide a phase diagram for these different phases as a function of particle size.

METHODS

Chemicals. Mercury chloride ($HgCl_2$, Sigma-Aldrich, 99%) (**Caution**: *Mercury compounds are highly toxic and should be handled with special care*), tellurium powder (Te, Sigma-Aldrich, 99.99%), silver nitrate (Alfa Aesar, 99.9%), SnO_2 nanoparticles (15% dispersion in water, Alfa Aesar), trioctylphosphine (TOP, Alfa Aesar, 90%), oleylamine (OLA, Acros, 80−90%), dodecanethiol (DDT, Sigma-Aldrich, 98%), ammonium chloride (Alfa Aesar, 98%), absolute ethanol (VWR), methanol (VWR, >98%), isopropanol (IPA, VWR), hexane (VWR, 99%), octane (Carlo erba, 99%), 2-mercaptoethanol (MPOH, Merck, >99%), *N*,*N*-dimethylformamide (DMF, VWR), *N*-methylformamide (NMF, Alfa Aesar, 99%), and toluene (VWR, 99.8%) are used in this study. All chemicals are used without further purification, except for oleylamine, which is centrifuged before use.

1 M TOP:Te Precursor. First, 2.54 g of Te powder is mixed in 20 mL of TOP in a three-neck flask. The flask is kept under vacuum at room temperature for 5 min, and then the temperature is increased to 100 °C. The flask is degassed for the next 20 min. The atmosphere is switched to nitrogen, and the temperature is increased to 275 °C. The solution is stirred until a clear orange color is obtained. The flask is cooled to room temperature, and the color changes to yellow. Finally, this solution is transferred to a nitrogen-filled glovebox for storage.

THz HgTe Nanocrystal Growth. First, 45 mL of oleylamine is introduced into a 100 mL three-neck flask, which is then placed under vacuum and heated to 120 °C for 1 h. Then, the solution is placed under a nitrogen atmosphere and heated to 200 °C. A second solution is made by mixing 270 mg of $HgCl_2$ and 1 mL of TOP:Te (1 M) in 5 mL of oleylamine. The mercury- and tellurium-containing solution is quickly injected (within 2 min of mixing) into the hot oleylamine flask. The color of the solution immediately turns to dark brown, and the reaction is carried out for 3 min. Then a mixture of 1 mL of dodecanethiol and 9 mL of chloroform is injected slowly into the flask to quench the reaction. The content of the flask is split over two tubes, and ethanol is added to precipitate the nanocrystals from the solution. The colorless supernatant is discarded, and the formed pellet is redispersed in 3 mL of chlorobenzene. The NCs are washed again with ethanol and redispersed in 3 mL of chlorobenzene. This process is repeated a third time.

For transmission electron microscopy (TEM) images, a drop of the NC solution is drop-casted onto a copper grid covered with an amorphous carbon film. The grid is degassed overnight to reduce future contamination. A JEOL 2010F instrument is used to acquire images and operated at 200 kV.

https://doi.org/10.1021/acs.jpclett.2c01636
J. Phys. Chem. Lett. 2022, 13, 6919−6926

Raman spectroscopy measurements are conducted at room temperature using a commercial confocal HORIBA LabRam HR Evolution micro-Raman microscope with a 100× objective and 532 nm laser excitation. Spectra are recorded between 50 and 400 cm^{-1} with 1800 lines/mm grating resulting in a resolution of 1 cm^{-1}. The spectrometer is calibrated using the 520.5 cm^{-1} band of a Si crystal. The effective laser power at the exit of the objective is ∼0.25 mW.

FTIR measurements at ambient pressure and room temperature are conducted in the ATR configuration of an Thermo Fisher IS50 FTIR spectrometer to characterize the grown particles. The source is a globar, the beam splitter a Si wafer, and the detector a DTGS apparatus. Acquisition is conducted with a 4 cm^{-1} resolution.

X-ray Photoemission Spectroscopy. The XPS measurements are conducted at the ANTARES beamline (SOLEIL synchrotron). A linear polarized light and a photon energy of 700 eV are used. The photoelectrons are collected with a new-generation MBS A-1 analyzer. The overall energy resolution is better than 60 meV. All XPS measurements are performed at room temperature. The binding energy is calibrated using the Au $4f_{7/2}$ photoemission peak that is set at 84.0 eV as an energy standard. For the deconvolution of the XPS spectra, a Shirley/linear background is subtracted and a Voight function with a 20% weighted Lorentzian contribution is used.

Electrode Fabrication. Si/SiO_2 wafers are cut with an edge size of 1 cm, cleaned by sonication in acetone, rinsed with acetone and isopropanol, and then subjected to a 5 min oxygen plasma cleaning. An adhesion primer (TI-PRIME) is spin-coated on the substrate, and the substrate baked at 120 °C for 120 s. Then, an AZ5214E resist is spin-coated and baked at 110 °C for 90 s. A MJB4 mask aligner is used to expose the substrates to ultraviolet light for 1.5 s through a lithography mask. Substrates are then baked at 125 °C for 2 min to invert the resist and flood-exposed (i.e., without a mask) for 40 s. The resist is developed using an AZ726 developer for 32 s and rinsed with pure water. Patterned substrates are dried and cleaned with 5 min of oxygen plasma to remove resist residues. In a thermal evaporator, 5 nm of chromium is deposited as an adhesion promoter before 80 nm of gold is evaporated. Lift-off is conducted in an acetone bath.

Film Deposition. We dissolve 30 mg of $HgCl_2$ in a solution of 18 mL of DMF and 2 mL of mercaptoethanol. The original solution of HgTe nanoparticles is treated to achieve ligand exchange. At each step, the solution is stirred with a vortex and sonicated. One milliliter of a HgTe nanocrystal solution is mixed with 1 mL of the exchange solution, and 5 mL of hexane and 1 mL of DMF are added to the solution. The top phase is then removed, and the solution is washed three more times adding 5 mL of hexane and removing the top phase each time. Finally, the solution is centrifugated for 5 min at 6000 rpm to precipitate the nanoparticles. The supernatant is discarded, and the formed pellet is dried under primary vacuum for 1 min and then redispersed in 100 μL of DMF to target a thickness of ∼150 nm. The obtained solution is called ink. Before the deposition of ink, the substrate is placed in an oxygen plasma cleaner for 2 min to promote adhesion. The ink is spin-coated on the substrate at 4000 rpm (at 2000 rpm s^{-1} acceleration) for 5 min. This leads to a homogeneous deposition between 100 and 200 nm.

Electrolyte Gating. For electrolyte gating, we first mix in a glovebox 0.5 g of $LiClO_4$ with 2.3 g of PEG (M_W = 10 kg mol^{-1}). The vial is heated at 170 °C on a hot plate for 2 h until the solution becomes clear. To use the electrolyte, the solution is warmed to ∼100 °C and brushed on the top of the HgTe film. The electrolyte is cooled to room temperature inside the glovebox, and a copper grid is then applied to it to ease the electrical contact.

Transport Measurements for Measurements Down to 15 K. The sample is glued using a silver paste on a substrate of silicon covered with a gold layer and mounted on the coldfinger of a cryostat. The gold layer is used as the gate contact when transistor measurements are conducted. The transfer curves and the IV curves are measured using a Keithley 2634B sourcemeter, which applies biases and measures currents.

Transport Measurements for Measurements Down to 2 K. A piece of alumina covered with a gold layer is glued to a sample holder using silver paste and electrically connected using microsoldering. The sample is glued using a silver paste on the gold layer and connected to the sample holder electrodes using silver paste. The gold layer is used as the gate contact when transistor properties are studied. The transfer curves and the IV curves are measured using two Keithley 2400 sourcemeters. The two instruments are used to drive the drain and gate while applying biases and measuring currents.

Thermoelectric Measurements. The sheet resistance of each film is measured using Keithley 2400 sourcemeters in the four-point van der Pauw configuration. The film thickness is measured by scratching the film and measuring the step height with a Veeco Dektak 150 profilometer. The electrical conductivity of the bulk film is calculated by multiplying the sheet resistance by the thickness of each film. The Seebeck coefficient (thermopower) is measured using a homemade probe setup in which the thin film sample is placed across two Peltier devices. A constant current is passed through the two Peltier devices that are placed ≈4 mm apart, which heats one side and cools the other, establishing a heat gradient across the sample. The temperature gradient (ΔT) is measured using two T-type thermocouples mounted in micromanipulators. The magnitude of the temperature gradient is directly correlated to the amount of current driven through the two Peltier devices. The induced open circuit voltage due to ΔT is measured using Keithley 2000 multimeters. Normally, within one measurement, eight different thermal gradients are established, and 10 voltage measurements are recorded and averaged at each ΔT. For all samples, the open circuit voltage exhibits a linear relationship with ΔT. The Seebeck coefficient is calculated by obtaining the slope of the plot of the voltage versus ΔT for each sample. Measurements are repeated and averaged. The electrical conductivity and Seebeck coefficient measurements are performed in a nitrogen-filled glovebox environment.

X-ray Diffraction under Pressure. Experiments are carried out using a membrane diamond anvil cell equipped with Boehler-Almax type anvils with 500 μm culets. A stainless-steel gasket with a thickness of 200 μm is preindented to 70 μm, provided with a 200 μm hole, and loaded with the sample, a 4:1 methanol/ethanol pressure-transmitting medium, and a 10 μm diameter ruby sphere that serves as a pressure marker. The "Mao hydrostatic" pressure scale is used to determine pressures. X-ray powder diffraction measurements are performed on a Rigaku MM007HF diffractometer equipped with a Mo rotating anode ($\lambda_{K\alpha1}$ = 0.709319 Å; $\lambda_{K\alpha2}$ = 0.713609 Å), Varimax focusing optics, and a RAXIS4++ image plate detector. X-ray data are collected at 20 °C. A LaB_6 standard sample is measured under the same experimental conditions to calibrate the Fit2D program, the image processing software

https://doi.org/10.1021/acs.jpclett.2c01636
J. Phys. Chem. Lett. 2022, 13, 6919−6926

used to integrate the intensities around the Debye−Scherrer rings and to obtain the one-dimensional patterns.

Infrared Spectroscopy under Pressure. Membrane diamond anvil cells (DACs), equipped with IIas-type Boehler-Almax diamond avils with 600 μm culets, are used. Stainless steel gaskets with a thickness of 200 μm are indented down to 50 μm. A 250 μm hole is then drilled by electro-erosion. The gasket is placed on the top of one of the anvils, and the gasket hole filled with CsI, using a far-infrared transparent pressure-transmitting medium. After the introduction of a ruby crystal, the DAC is closed under gentle pressure until the salt forms a clear window. One drop of a diluted suspension of NCs in chlorobenzene is then added and dried on top of the CsI window to form a dry and uniform film of NCs. The DAC is then closed and introduced into a liquid He flow cryostat enabling high-pressure measurements at low temperatures. The windows of the cryostat are made of polypropylene (PP) to optimize transmission in the far-infrared range, although some IR peaks of PP prevent measurement of a few narrow spectral regions in the mid-IR range. Then the cryostat is placed in a custom-made horizontal microscope available at the SMIS beamline of the synchrotron SOLEIL. The microscope is equipped with large working distance Schwarzschild objectives, allowing the incident infrared beam to be focused in the small optical aperture of the DAC inside the cryostat. The *in situ* pressure is monitored by the ruby luminescence technique, in which the signal is excited by a 532 nm laser and detected by an OceanOptics spectrometer, showing a characteristic doublet around 694 nm at ambient pressure. This photoluminescence is fitted, and the pressure is computed using the R1 peak position. Once the pressure is stabilized, an infrared absorbance spectrum is acquired using a Thermo Fisher Nicolet iS50 FTIR instrument with the synchrotron beam as the source. To acquire a broadband spectrum, we use a KBr beam splitter coupled to a MCT detector in the mid-IR range (for the 7500−600 cm^{-1} range), while we use a silicon beam splitter coupled with an InfraredLabs He-cooled bolometer for detection (for the 700−150 cm^{-1} range). This operation is repeated for various pressures from 0 to 10 GPa. When the maximum pressure is reached, the membrane is deflated and several spectra are acquired to check the reversibility of the pressure effect. The data processing procedure is described in Figure S8.

■ ASSOCIATED CONTENT

Supporting Information

The Supporting Information is available free of charge at https://pubs.acs.org/doi/10.1021/acs.jpclett.2c01636.

Material characterization, additional transport measurements at high temperatures, X-ray diffraction data and structural phase changes, a description of infrared spectrum acquisition and data processing and infrared spectra at low temperatures under pressure, and k.p modeling of the pressure dependence of the band gap in the zinc blende phase (PDF)

■ AUTHOR INFORMATION

Corresponding Author

Emmanuel Lhuillier − *Sorbonne Université, CNRS, Institut des NanoSciences de Paris, INSP, F-75005 Paris, France;* orcid.org/0000-0003-2582-1422; Email: el@insp.upmc.fr

Authors

Stefano Pierini − *Sorbonne Université, CNRS, Institut des NanoSciences de Paris, INSP, F-75005 Paris, France; Université Paris-Saclay, CNRS, Centre de Nanosciences et de Nanotechnologies, CNRS, 91120 Palaiseau, France;* orcid.org/0000-0003-1951-5357

Francesco Capitani − *Synchrotron SOLEIL, 91190 Saint-Aubin, France;* orcid.org/0000-0003-1161-7455

Michael Scimeca − *Department of Chemical and Biomolecular Engineering, New York University, Brooklyn, New York 11201, United States*

Sergei Kozlov − *Laboratoire de Physique et d'Etude des Matériaux, ESPCI-Paris, PSL Research University, Sorbonne Université Univ Paris 06, CNRS UMR 8213, 75005 Paris, France*

Debora Pierucci − *Université Paris-Saclay, CNRS, Centre de Nanosciences et de Nanotechnologies, CNRS, 91120 Palaiseau, France*

Rodolphe Alchaar − *Sorbonne Université, CNRS, Institut des NanoSciences de Paris, INSP, F-75005 Paris, France;* orcid.org/0000-0002-4734-4957

Claire Abadie − *Sorbonne Université, CNRS, Institut des NanoSciences de Paris, INSP, F-75005 Paris, France;* orcid.org/0000-0003-4309-9488

Adrien Khalili − *Sorbonne Université, CNRS, Institut des NanoSciences de Paris, INSP, F-75005 Paris, France;* orcid.org/0000-0001-5685-9963

Mariarosa Cavallo − *Sorbonne Université, CNRS, Institut des NanoSciences de Paris, INSP, F-75005 Paris, France;* orcid.org/0000-0002-8768-5545

Tung Huu Dang − *Sorbonne Université, CNRS, Institut des NanoSciences de Paris, INSP, F-75005 Paris, France;* orcid.org/0000-0003-0310-9004

Huichen Zhang − *Sorbonne Université, CNRS, Institut des NanoSciences de Paris, INSP, F-75005 Paris, France;* orcid.org/0000-0001-5346-0148

Erwan Bossavit − *Sorbonne Université, CNRS, Institut des NanoSciences de Paris, INSP, F-75005 Paris, France;* orcid.org/0000-0001-6088-3309

Charlie Gréboval − *Sorbonne Université, CNRS, Institut des NanoSciences de Paris, INSP, F-75005 Paris, France;* orcid.org/0000-0002-0314-7273

José Avila − *Synchrotron SOLEIL, 91190 Saint-Aubin, France*

Benoit Baptiste − *Sorbonne Université, CNRS, Institut de Minéralogie, de Physique des Matériaux et de Cosmochimie, IMPMC, F-75005 Paris, France*

Stefan Klotz − *Sorbonne Université, CNRS, Institut de Minéralogie, de Physique des Matériaux et de Cosmochimie, IMPMC, F-75005 Paris, France*

Ayaskanta Sahu − *Department of Chemical and Biomolecular Engineering, New York University, Brooklyn, New York 11201, United States;* orcid.org/0000-0002-1508-0213

Cheryl Feuillet-Palma − *Laboratoire de Physique et d'Etude des Matériaux, ESPCI-Paris, PSL Research University, Sorbonne Université Univ Paris 06, CNRS UMR 8213, 75005 Paris, France*

Xiang Zhen Xu − *Laboratoire de Physique et d'Etude des Matériaux, ESPCI-Paris, PSL Research University, Sorbonne Université Univ Paris 06, CNRS UMR 8213, 75005 Paris, France*

Abdelkarim Ouerghi − *Université Paris-Saclay, CNRS, Centre de Nanosciences et de Nanotechnologies, CNRS, 91120 Palaiseau, France;* orcid.org/0000-0002-1898-2765

https://doi.org/10.1021/acs.jpclett.2c01636
J. Phys. Chem. Lett. 2022, 13, 6919−6926

Sandrine Ithurria − *Laboratoire de Physique et d'Etude des Matériaux, ESPCI-Paris, PSL Research University, Sorbonne Université Univ Paris 06, CNRS UMR 8213, 75005 Paris, France;* orcid.org/0000-0002-4733-9883

James K. Utterback − *Sorbonne Université, CNRS, Institut des NanoSciences de Paris, INSP, F-75005 Paris, France;* orcid.org/0000-0002-2926-841X

Sebastien Sauvage − *Université Paris-Saclay, CNRS, Centre de Nanosciences et de Nanotechnologies, CNRS, 91120 Palaiseau, France;* orcid.org/0000-0001-8132-1372

Complete contact information is available at: https://pubs.acs.org/10.1021/acs.jpclett.2c01636

Notes

The authors declare no competing financial interest.

■ ACKNOWLEDGMENTS

The project is supported by ERC starting grant blackQD (Grant 756225). The authors acknowledge the use of clean-room facilities of "Centrale de Proximité Paris-Centre". This work has been supported by the Region Ile-de-France in the framework of DIM Nano-K (Grant dopQD). This work was supported by French state funds managed by the ANR within the Investissements d'Avenir program under reference ANR-11-IDEX-0004-02 and more specifically within the framework of the Cluster of Excellence MATISSE and also by grants from IPER-Nano2 (ANR-18CE30-0023-01), Copin (ANR-19-CE24-0022), Frontal (ANR-19-CE09-0017), Graskop (ANR-19-CE09-0026), NITQuantum (ANR-20-ASTR-0008-01), Bright (ANR-21-CE24-0012-02), MixDferro (ANR-21-CE09-0029), and Quickterra (ANR-22-CE09). M.S. and A.S. acknowledge support by the U.S. National Science Foundation under Grant ECCS-1809064 and the U.S. Department of Defense Office of Naval Research under Grant N00014-20-1-2231, respectively.

■ REFERENCES

(1) Gréboval, C.; Chu, A.; Goubet, N.; Livache, C.; Ithurria, S.; Lhuillier, E. Mercury Chalcogenide Quantum Dots: Material Perspective for Device Integration. *Chem. Rev.* **2021**, *121*, 3627−3700.

(2) Kershaw, S. V.; Rogach, A. L. Infrared Emitting HgTe Quantum Dots and Their Waveguide and Optoelectronic Devices. *Z. Für Phys. Chem.* **2015**, *229*, 23−64.

(3) Geiregat, P.; Houtepen, A. J.; Sagar, L. K.; Infante, I.; Zapata, F.; Grigel, V.; Allan, G.; Delerue, C.; Van Thourhout, D.; Hens, Z. Continuous-Wave Infrared Optical Gain and Amplified Spontaneous Emission at Ultralow Threshold by Colloidal HgTe Quantum Dots. *Nat. Mater.* **2018**, *17*, 35−42.

(4) Qu, J.; Weis, M.; Izquierdo, E.; Mizrahi, S. G.; Chu, A.; Dabard, C.; Gréboval, C.; Bossavit, E.; Prado, Y.; Péronne, E.; et al. Electroluminescence from Nanocrystals above 2 μm. *Nat. Photonics* **2022**, *16*, 38−44.

(5) Shen, X.; Peterson, J. C.; Guyot-Sionnest, P. Mid-Infrared HgTe Colloidal Quantum Dot LEDs. *ACS Nano* **2022**, *16*, 7301−7308.

(6) Bossavit, E.; Qu, J.; Abadie, C.; Dabard, C.; Dang, T.; Izquierdo, E.; Khalili, A.; Gréboval, C.; Chu, A.; Pierini, S.; et al. Optimized Infrared LED and Its Use in an All-HgTe Nanocrystal-Based Active Imaging Setup. *Adv. Opt. Mater.* **2022**, *10*, 2101755.

(7) Chen, M.; Lu, H.; Abdelazim, N. M.; Zhu, Y.; Wang, Z.; Ren, W.; Kershaw, S. V.; Rogach, A. L.; Zhao, N. Mercury Telluride Quantum Dot Based Phototransistor Enabling High-Sensitivity Room-Temperature Photodetection at 2000 nm. *ACS Nano* **2017**, *11*, 5614−5622.

(8) Gréboval, C.; Chu, A.; Magalhaes, D. V.; Ramade, J.; Qu, J.; Rastogi, P.; Khalili, A.; Chee, S.-S.; Aubin, H.; Vincent, G.; et al. Ferroelectric Gating of Narrow Band-Gap Nanocrystal Arrays with Enhanced Light−Matter Coupling. *ACS Photonics* **2021**, *8*, 259−268.

(9) Gréboval, C.; Noumbe, U.; Goubet, N.; Livache, C.; Ramade, J.; Qu, J.; Chu, A.; Martinez, B.; Prado, Y.; Ithurria, S.; et al. Field-Effect Transistor and Photo-Transistor of Narrow-Band-Gap Nanocrystal Arrays Using Ionic Glasses. *Nano Lett.* **2019**, *19*, 3981−3986.

(10) Noumbé, U. N.; Gréboval, C.; Livache, C.; Chu, A.; Majjad, H.; Parra López, L. E.; Mouafo, L. D. N.; Doudin, B.; Berciaud, S.; Chaste.; et al. Reconfigurable 2D/0D p−n Graphene/HgTe Nanocrystal Heterostructure for Infrared Detection. *ACS Nano* **2020**, *14*, 4567−4576.

(11) Chu, A.; Gréboval, C.; Goubet, N.; Martinez, B.; Livache, C.; Qu, J.; Rastogi, P.; Bresciani, F. A.; Prado, Y.; Suffit, S.; et al. Near Unity Absorption in Nanocrystal Based Short Wave Infrared Photodetectors Using Guided Mode Resonators. *ACS Photonics* **2019**, *6*, 2553−2561.

(12) Tang, X.; Ackerman, M. M.; Guyot-Sionnest, P. Thermal Imaging with Plasmon Resonance Enhanced HgTe Colloidal Quantum Dot Photovoltaic Devices. *ACS Nano* **2018**, *12*, 7362−7370.

(13) Zhu, B.; Chen, M.; Zhu, Q.; Zhou, G.; Abdelazim, N. M.; Zhou, W.; Kershaw, S. V.; Rogach, A. L.; Zhao, N.; Tsang, H. K. Integrated Plasmonic Infrared Photodetector Based on Colloidal HgTe Quantum Dots. *Adv. Mater. Technol.* **2019**, *4*, 1900354.

(14) Dang, T. H.; Abadie, C.; Khalili, A.; Gréboval, C.; Zhang, H.; Prado, Y.; Xu, X. Z.; Gacemi, D.; Descamps-Mandine, A.; Ithurria, S.; et al. Broadband Enhancement of Mid-Wave Infrared Absorption in a Multi-Resonant Nanocrystal-Based Device. *Adv. Opt. Mater.* **2022**, *10*, 2200297.

(15) Ciani, A. J.; Pimpinella, R. E.; Grein, C. H.; Guyot-Sionnest, P. Colloidal Quantum Dots for Low-Cost MWIR Imaging. In *Infrared Technology and Applications XLII*; SPIE, 2016; Vol. *9819*, pp 333−341.

(16) Gréboval, C.; Darson, D.; Parahyba, V.; Alchaar, R.; Abadie, C.; Noguier, V.; Ferré, S.; Izquierdo, E.; Khalili, A.; Prado.; et al. Photoconductive Focal Plane Array Based on HgTe Quantum Dots for Fast and Cost-Effective Short-Wave Infrared Imaging. *Nanoscale* **2022**, *14*, 9359−9368.

(17) Chu, A.; Martinez, B.; Ferré, S.; Noguier, V.; Gréboval, C.; Livache, C.; Qu, J.; Prado, Y.; Casaretto, N.; Goubet, N.; et al. HgTe Nanocrystals for SWIR Detection and Their Integration up to the Focal Plane Array. *ACS Appl. Mater. Interfaces* **2019**, *11*, 33116−33123.

(18) Guzelturk, B.; Trigo, M.; Delaire, O.; Reis, D. A.; Lindenberg, A. M. Dynamically Tunable Terahertz Emission Enabled by Anomalous Optical Phonon Responses in Lead Telluride. *ACS Photonics* **2021**, *8*, 3633−3640.

(19) Goubet, N.; Jagtap, A.; Livache, C.; Martinez, B.; Portalès, H.; Xu, X. Z.; Lobo, R. P. S. M.; Dubertret, B.; Lhuillier, E. Terahertz HgTe Nanocrystals: Beyond Confinement. *J. Am. Chem. Soc.* **2018**, *140*, 5033−5036.

(20) Rinnerbauer, V.; Hingerl, K.; Kovalenko, M.; Heiss, W. Effect of Quantum Confinement on Higher Transitions in HgTe Nanocrystals. *Appl. Phys. Lett.* **2006**, *89*, 193114.

(21) Choi, D.; Yoon, B.; Kim, D.-K.; Baik, H.; Choi, J.-H.; Jeong, K. S. Major Electronic Transition Shift from Bandgap to Localized Surface Plasmon Resonance in $Cd_xHg_{1-X}Se$ Alloy Nanocrystals. *Chem. Mater.* **2017**, *29*, 8548−8554.

(22) Kim, J.; Choi, D.; Seob Jeong, K. Self-Doped Colloidal Semiconductor Nanocrystals with Intraband Transitions in Steady State. *Chem. Commun.* **2018**, *54*, 8435−8445.

(23) Jagtap, A.; Livache, C.; Martinez, B.; Qu, J.; Chu, A.; Gréboval, C.; Goubet, N.; Lhuillier, E. Emergence of Intraband Transitions in Colloidal Nanocrystals. *Opt. Mater. Express* **2018**, *8*, 1174−1183.

(24) Sahu, A.; Khare, A.; Deng, D. D.; Norris, D. J. Quantum Confinement in Silver Selenide Semiconductor Nanocrystals. *Chem. Commun.* **2012**, *48*, 5458−5460.

(25) Scimeca, M. R.; Mattu, N.; Paredes, I. J.; Tran, M. N.; Paul, S. J.; Aydil, E. S.; Sahu, A. Origin of Intraband Optical Transitions in

Ag_2Se Colloidal Quantum Dots. *J. Phys. Chem. C* **2021**, *125*, 17556−17564.
(26) Apretna, T.; Massabeau, S.; Gréboval, C.; Goubet, N.; Tignon, J.; Dhillon, S.; Carosella, F.; Ferreira, R.; Lhuillier, E.; Mangeney, J. Few Picosecond Dynamics of Intraband Transitions in THz HgTe Nanocrystals. *Nanophotonics* **2021**, *10*, 2753−2763.
(27) Ruppert, M.; Bui, H.; Sagar, L. K.; Geiregat, P.; Hens, Z.; Bester, G.; Huse, N. Intraband Dynamics of Mid-Infrared HgTe Quantum Dots. *Nanoscale* **2022**, *14*, 4123−4130.
(28) Moghaddam, N.; Gréboval, C.; Qu, J.; Chu, A.; Rastogi, P.; Livache, C.; Khalili, A.; Xu, X. Z.; Baptiste, B.; Klotz, S.; et al. The Strong Confinement Regime in HgTe Two-Dimensional Nanoplatelets. *J. Phys. Chem. C* **2020**, *124*, 23460−23468.
(29) Saini, P. K.; Singh, D.; Ahlawat, D. S. Calculations of Electronic Band Structure and Optical Properties of HgTe under Pressure. *Indian J. Pure Appl. Phys.* **2017**, *55*, 649−654.
(30) Chen, X.; Wang, Y.; Cui, T.; Ma, Y.; Zou, G.; Iitaka, T. HgTe: A Potential Thermoelectric Material in the Cinnabar Phase. *J. Chem. Phys.* **2008**, *128*, 194713.
(31) Duz, I.; Kart, H. H.; Kart, S. O.; Kuzucu, V. Theoretical Investigations on HgTe Chalcogenide Materials under High Pressure. *Phys. Scr.* **2021**, *96*, 045703.
(32) Krishtopenko, S. S.; Yahniuk, I.; But, D. B.; Gavrilenko, V. I.; Knap, W.; Teppe, F. Pressure- and Temperature-Driven Phase Transitions in HgTe Quantum Wells. *Phys. Rev. B* **2016**, *94*, 245402.
(33) Martinez, B.; Livache, C.; Notemgnou Mouafo, L. D.; Goubet, N.; Keuleyan, S.; Cruguel, H.; Ithurria, S.; Aubin, H.; Ouerghi, A.; Doudin.; et al. HgSe Self-Doped Nanocrystals as a Platform to Investigate the Effects of Vanishing Confinement. *ACS Appl. Mater. Interfaces* **2017**, *9*, 36173−36180.
(34) Martinez, B.; Ramade, J.; Livache, C.; Goubet, N.; Chu, A.; Gréboval, C.; Qu, J.; Watkins, W. L.; Becerra, L.; Dandeu, E.; et al. HgTe Nanocrystal Inks for Extended Short-Wave Infrared Detection. *Adv. Opt. Mater.* **2019**, *7*, 1900348.
(35) Lan, X.; Chen, M.; Hudson, M. H.; Kamysbayev, V.; Wang, Y.; Guyot-Sionnest, P.; Talapin, D. V. Quantum Dot Solids Showing State-Resolved Band-like Transport. *Nat. Mater.* **2020**, *19*, 323−329.
(36) Zabet-Khosousi, A.; Dhirani, A.-A. Charge Transport in Nanoparticle Assemblies. *Chem. Rev.* **2008**, *108*, 4072−4124.
(37) Baars, J.; Sorger, F. Reststrahlen Spectra of HgTe and $Cd_xHg_{1-X}Te$. *Solid State Commun.* **1972**, *10*, 875−878.
(38) San-Miguel, A.; Wright, N. G.; McMahon, M. I.; Nelmes, R. J. Pressure Evolution of the Cinnabar Phase of HgTe. *Phys. Rev. B* **1995**, *51*, 8731−8736.
(39) Tolbert, S. H.; Alivisatos, A. P. Size Dependence of a First Order Solid-Solid Phase Transition: The Wurtzite to Rock Salt Transformation in CdSe Nanocrystals. *Science* **1994**, *265*, 373−376.
(40) Jacobs, K.; Wickham, J.; Alivisatos, A. P. Threshold Size for Ambient Metastability of Rocksalt CdSe Nanocrystals. *J. Phys. Chem. B* **2002**, *106*, 3759−3762.
(41) Jacobs, K.; Zaziski, D.; Scher, E. C.; Herhold, A. B.; Paul Alivisatos, A. Activation Volumes for Solid-Solid Transformations in Nanocrystals. *Science* **2001**, *293*, 1803−1806.
(42) Tolbert, S. H.; Alivisatos, A. P. The Wurtzite to Rock Salt Structural Transformation in CdSe Nanocrystals under High Pressure. *J. Chem. Phys.* **1995**, *102*, 4642−4656.
(43) Zhang, H.; Zhang, G.; Wang, J.; Wang, Q.; Zhu, H.; Liu, C. Structural and Electrical Transport Properties of PbS Quantum Dots under High Pressure. *J. Alloys Compd.* **2021**, *857*, 157482.
(44) Bian, K.; Richards, B. T.; Yang, H.; Bassett, W.; Wise, F. W.; Wang, Z.; Hanrath, T. Optical Properties of PbS Nanocrystal Quantum Dots at Ambient and Elevated Pressure. *Phys. Chem. Chem. Phys.* **2014**, *16*, 8515−8520.
(45) Livache, C.; Goubet, N.; Gréboval, C.; Martinez, B.; Ramade, J.; Qu, J.; Triboulin, A.; Cruguel, H.; Baptiste, B.; Klotz, S.; et al. Effect of Pressure on Interband and Intraband Transition of Mercury Chalcogenide Quantum Dots. *J. Phys. Chem. C* **2019**, *123*, 13122−13130.
(46) Ohtani, A.; Seike, T.; Motobayashi, M.; Onodera, A. The Electrical Properties of HgTe and HgSe under Very High Pressure. *J. Phys. Chem. Solids* **1982**, *43*, 627−632.
(47) Li, Q.; Zhang, J.; Zheng, Q.; Guo, W.; Cao, J.; Jin, M.; Zhang, X.; Li, N.; Wu, Y.; Ye, X.; et al. Pressure-Induced Superconductivity in HgTe Single-Crystal Film. *Adv. Sci.* **2022**, *9*, 2200590.

https://doi.org/10.1021/acs.jpclett.2c01636
J. Phys. Chem. Lett. 2022, 13, 6919−6926